Available online at www.sciencedirect.com
SCIENCE DIRECT®
PERGAMON
International Journal of Heat and Mass Transfer 46 (2003) 4639–4656
International Journal of HEAT and MASS TRANSFER
www.elsevier.com/locate/ijhmt

Characteristics of vortex flow in a low speed air jet impinging onto a heated disk in a vertical cylindrical chamber

J.C. Hsieh, T.C. Cheng, T.F. Lin *

Department of Mechanical Engineering, National Chiao Tung University, Hsinchu 30010, Taiwan, ROC

Received 23 December 2002; received in revised form 29 May 2003

Abstract

An experiment combining flow visualization and transient temperature measurement is carried out to investigate the characteristics of the mixed convective vortex flow resulting from a low speed air jet impinging onto a heated horizontal circular disk confined in a vertical adiabatic cylindrical chamber. Attention is focused on the conditions leading to the onset of the inertia and buoyancy driven vortex rolls and the effects of governing nondimensional groups on the steady and time dependent vortex flow. More specifically, experiments are conducted for the jet Reynolds number varied from 0 to 1082 and Rayleigh number from 0 to 18,790 for two different injection pipes. The results show that typically the steady vortex flow in the processing chamber consists of two inertia-driven and one buoyancy-driven circular vortex rolls. The secondary inertia-driven roll only appears at high jet Reynolds numbers. At low buoyancy-to-inertia ratio Gr/Re_j^2 the vortex rolls are steady and axisymmetric. But at certain high Gr/Re_j^2 the vortex flow becomes unstable and the vortex rolls are somewhat deformed. Besides, new vortex rolls can be induced by the additional thermal rising from the heated disk and the splitting of the primary inertia-driven roll. The temporal characteristics of the time periodic vortex flows are examined in detail. In the region dominated by the new rolls the flow oscillates significantly. Finally, empirical equations are proposed to correlate the oscillation frequency of the time periodic flow, and the size and location of the vortex rolls. Furthermore, the conditions for the onset of the buoyancy driven rolls are given. A flow regime map is provided to delineate the temporal state of the vortex flow.

1. Introduction

Flow and heat transfer associated with a jet impinging onto a large heated flat plate have been the subject of many investigations because of its superior heat transfer capability. The results [1] have been applied to improve the drying of textiles and paper, annealing of glass, cooling of gas turbine components and microelectronic equipments, freezing of tissue in cryosurgery, etc. However, for application such as chemical vapor deposition (CVD) [2], the radial uniformity of heat and mass transfer rate on the plate is relatively important. Besides, the flow needs to be stable and contain no vortices. The interest in the impinging jet confined in a chamber has accelerated recently because of the quick technological progresses in the growth of semiconductor thin crystal films through rapid thermal processing (RTP) [3] and CVD [4]. Particularly, the flow recirculation in the processing chamber is detrimental to the film properties. But, the associated detailed vortex flow characteristics remain largely unexplored. In an attempt to examine the flow recirculation in the RTP processes we recently visualized the vortex flow in a model vertical RTP processor [5] and found that the flow was dominated by the two circular rolls, an inertia-driven roll and a buoyancy-driven roll. The effects of the jet flow rate, temperature difference between the substrate and air jet, and chamber pressure on the vortex flow pattern were investigated in detail. In the present study a completely new experimental system with more

* Corresponding author. Tel.: +886-35712121; fax: +886-35726440.
E-mail address: t7217@cc.nctu.edu.tw (T.F. Lin).

0017-9310/$ - see front matter © 2003 Elsevier Ltd. All rights reserved.
doi:10.1016/S0017-9310(03)00304-1

Nomenclature

D_j	jet diameter at the injection pipe exit (mm)
f	oscillation frequency of time periodic flow (Hz)
F	nondimensional oscillation frequency, $f/(\alpha/H^2)$
g	gravitational acceleration (m/s^2)
Gr	Grashof number, $g\beta\Delta TH^3/v^2$
H	distance between the exit of injection pipe and heated plate (mm)
Q_j	jet flow rate (standard liter per minute, slpm)
r_s	the center of the location of secondary inertia-driven roll (mm)
r,θ,z	dimensional cylindrical coordinates
R,Θ,Z	dimensionless cylindrical coordinates, $r/R_c,\theta,z/H$
Ra	Rayleigh number, $g\beta\Delta TH^3/\alpha v$
R_c	radius of processing chamber (mm)
Re_j	jet Reynolds number, $\overline{V_j}D_j/v$ or $4Q_j/\pi vD_j$
S_I	size of primary inertia-driven roll (mm)
S_O	size of buoyancy-driven roll (mm)
T_f	temperature of the heated disk (°C)
T_j	temperature of jet at the injection pipe exit (°C)
t	time (s)
$\overline{V_j}$	average velocity of the air jet at the injection pipe exit (m/s)

Greek symbols

α	thermal diffusivity (cm^2/s)
β	thermal expansion coefficient (K^{-1})
ΔT	temperature difference between the heated disk and the injected air (°C)
v	kinematic viscosity (cm^2/s)
Φ	nondimensional temperature, $(T-T_j)/(T_f-T_j)$

precise flow and temperature control of the jet and substrate is established to explore the roles of the inertia and buoyancy forces in affecting the vortex rolls. In particular, with the experiment conducted in this improved system the onset and the characteristics of the inertia and buoyancy driven steady and unsteady vortex flow structures can be captured and will be examined in detail.

Considerable research has been carried out in the past to study the fluid flow and heat transfer in the round or slot jet impinging onto a large horizontal plate. Most of the studies focus on quantifying the highly efficient heat transfer associated with the high speed impinging jets and the jets considered possess a much higher inertia than the buoyancy force generated by the temperature nonuniformity in the flow. Therefore the jet impinging flow is dominated by the jet inertia. For instances, heat or mass transfer in the laminar and turbulent impinging jets was experimentally investigated by Scholtz and Trass [6], Sparrow and Wong [7], Masliyah and Nguyen [8], and Hrycak [9]. Recently, the flow and thermal structures of the turbulent round jets were examined by Özdermir and Whitelaw [10] and Liu and Sullivan [11]. Moreover, the laminar impinging jets with an upper plate confinement were numerically predicted by Saad et al. [12] and Law and Masliyah [13].

The presence of a confinement plate above the target plate was noted to induce a big flow recirculation around the jet axis [14–16]. The characteristics of the recirculation were influenced by the jet Reynolds number Re_j and nozzle-to-plate spacing H [17,18]. They revealed that the center of the flow recirculation moved away from the jet axis at increasing H. The confinement plate can also restrict the flow entrainment from the surrounding, which reduces the jet spreading rate and leads to a longer potential core [19]. Moreover, the flow in a confined impinging jet is dominated by a large recirculation vortex around the jet axis and a comparatively smaller adjacent secondary vortex right above the impinging plate [13,20]. More recently, for a confined laminar impinging jet ($Re_j < 1000$) the critical jet Reynolds number for the onset of unsteady flow was numerically shown to be between 585 and 610 [21]. The unsteady jet was characterized by a dominant frequency corresponding to the formation of shear layer vortices at the jet exit. More complete information on the impinging jets can be found from the critical reviews by Viskanta [22] and Jambunathan et al. [23].

In the impinging jet flow confined in a chamber encountered in the CVD and RTP processes, the gases input to the CVD and RTP chamber are at relatively low flow rates and the wafer upon which thin crystal films are grown and processed is at an elevated temperature with the Reynolds and Rayleigh numbers respectively ranging from 1.0 to 100 and from 0 to 10^5 [4]. Under such circumstance the buoyancy in the flow is no longer small compared with the jet inertia. Significant flow recirculation can be induced by the buoyancy and the impinging jet flow is driven by the combined effects of the inertia and buoyancy. The importance of the buoyancy on the recirculating flow in a vertical CVD reactor was demonstrated by Wahl [24]. Similar investigations

have been carried out for various types of CVD reactors including the metal organic CVD [25–27] and single-wafer RTP processors [28]. In these studies for the processing of the microelectronic circuits [24–28] various vortex flow patterns were reported in the jet impinging flow. Buoyancy induced symmetry breaking of the jet flow was also noted [27].

The above literature review clearly reveals that the detailed vortex flow characteristics associated with a mixed convective low speed round gas jet impinging onto a heated circular plate in a confined chamber are not well understood. In this study an experimental system is established to delineate how the inertia and buoyancy forces affect the vortex flow patterns in this confined impinging jet flow. Attention is focused on the effects of the jet flow rate, temperature difference between the heated plate and jet, and diameter of the injection pipe on the steady and unsteady vortex flow patterns and their onset.

2. Experimental apparatus and procedures

In order to conduct the experiment at reasonably low cost, we use air as the working fluid to replace the inert gases normally employed in real CVD and RTP processes. In view of the similar thermodynamic and thermophysical properties for various gases, the results obtained here are still applicable to the CVD and RTP systems. A completely new experimental system is established here, which is not improved from the one used in the previous study [5], to investigate the vortex flow resulting from a round jet impinging vertically downwards onto a circular heated disk confined in a vertical cylindrical chamber. The system and the test section are schematically shown in Figs. 1 and 2. The experimental system consists of four major parts—the processing chamber, temperature measurement and data acquisition unit, heating unit, and gas injection unit. The major parts are briefly described in the following.

The processing chamber, which is made of 6-mm thick quartz glass to allow for the observation of the vortex flow pattern in it, is cylindrical and has a diameter of 291 mm and height of 200 mm. Air is injected vertically downward from a long straight circular pipe into the cylindrical chamber along the axis of the chamber and impinges directly onto the heated disk. The air flows first over the heated disk, then moves through the annular section of the chamber, and finally leaves the chamber via 20 circular outlets of 12.7 mm in diameter opened at the bottom of the chamber. The chamber is sealed to prevent any gas leakage. The top, bottom and side walls of the chamber are thermally well insulated to reduce the heat loss from the processing chamber to the ambient during the experiment. More specifically, the entire chamber is insulated with a superlon insulator of 100-mm thick. The insulator can be opened during the flow visualization.

The heating unit is designed to maintain the circular disk at the preset uniform temperature during the experiment. The disk is a 25-mm thick high purity circular copper plate of 8-in. in diameter. The heater attached onto the backside of the copper plate is divided into three concentric zones. Each zone is independently heated by a DC power supply with a DC current passing through the nickel coil placed on a stainless steel base. Additionally, to reduce the heat loss from the sidewall of the copper plate and stainless steel base, the lateral surface of the entire heating unit is wrapped with a 16-mm thick thermal insulation layer of superlon. Care is taken to insure that the outside surface of the insulation layer is smooth and cylindrical. The entire heating unit is then placed on a Teflon plate. Moreover, the copper plate temperature is measured by six corrected and calibrated T-type thermocouples at selected detection points located at 1-mm below the upper surface of the copper plate, which are inserted into the plate through the small holes drilled from the backside of the plate. A proper control of the voltage from each power supply allows us to maintain the surface of the copper plate at a nearly uniform temperature. The measured data indicate that the uncertainty in maintaining the copper plate temperature is ± 0.1 °C. No bias in the plate temperature is noted and the temperature nonuniformity is spatially random.

The gas injection unit consists of a 2HP air compressor, a flow meter, a smoke generator, filters, pressure regulator, connection pipe and injection pipe. In the experiment, air is drawn from the ambient by the compressor and sent into a 300-l and 100-psi high-pressure air tank and is filtered to remove moisture and tiny particles. The installation of the high-pressure air tank intends to suppress the fluctuation of the air flow and extends the life of the compressor. Then, the air is mixed with smoke tracers in the smoke generator and regulated by the pressure regulator. It is later injected into the processing chamber through the straight circular injection pipe which is coaxial with the processing chamber. The downward vertical air jet issuing from the pipe outlet impinges directly onto the heated plate. In the present study, two injection pipes with diameters 10.0 and 22.1 mm are tested and the straight portions of the pipes are both 600.0-mm long. This length of the injection pipes is selected to ensure that they are long enough for the flow to become fully developed before reaching the exit of the injection pipe. The distance between the injection pipe exit and the heated disk is 20.0 mm. The air temperature at 600.0-mm upstream of the injection pipe exit is measured by a T-type thermocouple. The measured value is considered as the temperature of the air injected into the processing chamber since the whole

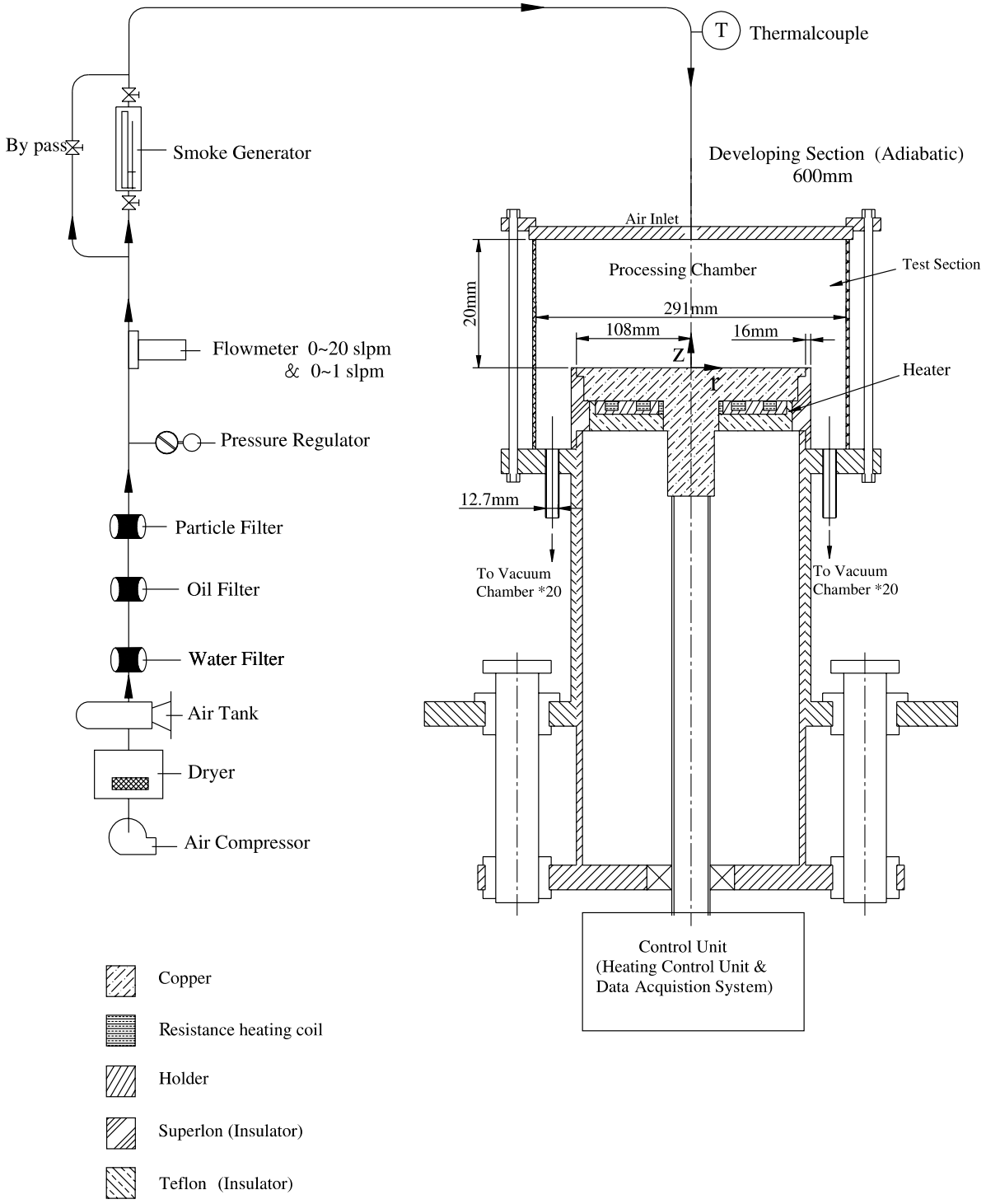

Fig. 1. Schematic diagram of the experimental system.

injection pipe is thermally well insulated by a 16-mm layer of superlon.

A smoke-tracer flow visualization technique is employed to observe the flow patterns in the cylindrical

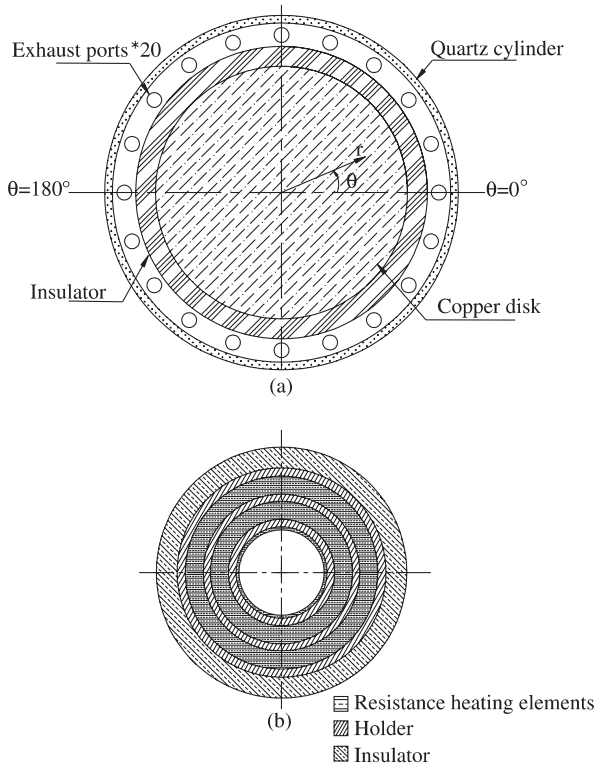

Fig. 2. Schematic of the test section from the top view (a) and 3-zone concentric heater (b).

chamber. The gas flow pattern is illuminated by vertical and horizontal plane light sheets produced by passing parallel light sheets from an overhead projector through adjustable knife edges. The experimental system is located in a darkroom to improve the contrast of the flow photos. The time variations of the flow pattern during the entire transient stage from the top and side views are recorded by the Sony digital video camera DCR-PC100. The recorded images are later examined carefully in a personal computer. The air temperature at selected locations in the processing chamber is measured by a thermocouple probe which is inserted into the chamber through the small holes opened at the chamber top. The probe is an OMEGA (model HYPO) mini hypodermic extremely small T-type thermocouple implanted in a 1-in. long stainless steel hypodermic needle.

For each case the experiment starts with the air at the room temperature compressed first into the smoke generator through the connection pipe and then injected into the processing chamber. The air moves over the heated disk and finally leaves the chamber through the outlets at the bottom of the chamber. In the meantime the temperature of the disk and the air flow rate are controlled at the preset levels. As the mixed convective air flow in the processing chamber reaches steady or statistically stable state, we begin to visualize the vortex flow pattern in the chamber.

Uncertainties in the Rayleigh number, Reynolds number and other independent parameters are calculated according to the standard procedures established by Kline and McClintock [29]. The uncertainties of the thermophysical properties of the air are included in the analysis. The properties of the working fluid (air) are $\alpha = 0.22$ (cm^2/s), $\beta = 0.0034$ (K^{-1}), $v = 0.16$ (cm^2/s) and $Pr = 0.72$ at 30 °C and 1.0 bar. In addition, the uncertainties of the control unsteadiness and temperature nonuniformity are accounted for in the evaluation of the data uncertainty. The analysis shows that the uncertainties of temperature, volume flow rate, dimensions, Reynolds number and Rayleigh number measurements are estimated to be less than ±0.2 °C, ±2%, ±0.05 mm, 2% and 4%, respectively.

To validate our experimental setup, the flow observed in the processing chamber for the limiting case when the disk is unheated ($Ra = 0$) is compared with the numerical results from Law and Masliyah [13] for the impinging jet flow with a top plate confinement but without the sidewall confinement. It is noted that in the region surrounding the jet axis the resulting vortex flow from our flow visualization is nearly the same as their numerical prediction.

3. Results and discussion

In the present experiment the air flow rate Q_j is varied from 0 to 5 slpm (standard liter per minute) and temperature difference between the heated disk and injected air ΔT is varied form 0 to 25 °C for two injection pipes with $D_j = 10.0$ and 22.1 mm. The ranges of the parameters chosen above are in accordance with the values of the governing dimensionless groups for the flow often encountered in the CVD processes [4]. The dimensionless groups governing the present problem are the jet Reynolds and Rayleigh numbers, defined as

$$Re_j = \overline{V}_j D_j/\nu = 4Q_j/\pi\nu D_j \quad (1)$$

and

$$Ra = g\beta\Delta TH^3/\alpha\nu \quad (2)$$

In this study Re_j and Ra range respectively from 0 to 1082 and 0 to 18,790. At this low jet Reynolds number the impinging jet when unheated is laminar and steady [21]. In what follows selected flow photos from the top and side views are examined closely to unravel various aspects of the vortex flow in the processing chamber. In addition, the data from the temperature measurement are presented to illustrate the transient characteristics of the flow.

3.1. Typical steady flow pattern

At first, the typical vortex flow pattern in the processing chamber with the small injection pipe ($D_j = 10.0$ mm) at long time when the flow already reaches steady state at a low buoyancy–inertia ratio Gr/Re_j^2, which is also known as the Richardson number, is illustrated in Fig. 3. Here, the steady flow photos from the top and side views taken respectively at the selected horizontal and vertical planes along with the schematic sketch of the flow for a typical case with $Q_j = 3.0$ slpm and $\Delta T = 9.9$ °C ($Re_j = 406$, $Ra = 7440$ and $Gr/Re_j^2 = 0.045$) are shown. Since the flow is axisymmetric at this low Gr/Re_j^2, only a half of the top view flow photo and the side view flow photo at the vertical plane $\theta = 0°$ and 180° are given here. Examining the top and side view photos together reveals that the steady vortex flow pattern in the processing chamber is characterized by three circular vortex rolls. The first (inner) circular roll directly surrounds the downward air jet and is much larger than the second vortex roll induced in the middle zone of the chamber. The third (outer) roll is also large in size and occupies the outer zone of the chamber. A close inspection of the successive top and side view flow photos stored in the video tapes indicates that immediately after the impinging, the jet is deflected by the heated disk to move obliquely upwards (Fig. 3(c)). Then the oblique flow is divided into two streams as it encounters the chamber top. One stream moves radially inwards towards the low pressure region created by the jet injection forming the inner toroidal vortex, which is considered as the primary inertia-driven vortex roll. Meanwhile, the inner roll can be formed from the air entrained by the jet injected into the chamber. Another stream moves radially outwards, later turns to move downwards along the sidewall of chamber, and finally leave the chamber through the outlets in the chamber bottom. Besides, the smaller second circular roll is found to be induced through the viscous shearing effects produced by the inner vortex roll, which is therefore termed as the secondary inertia-driven roll. It should be mentioned that this secondary roll is induced only when the jet Reynolds number exceeds certain level around 180 for the smaller injection pipe with $Ra = 0$. Moreover, the outer roll near the chamber side is driven by the buoyancy force associated with the heated disk and is regarded as the buoyancy-driven roll.

3.2. Onset of vortex flow

Understanding of the critical condition for the appearance of the inertia- and buoyancy-driven vortex rolls in the chamber is of fundamental interest in the fluid flow study. Here we investigate the onset of the inertia-driven rolls by visualizating the flow at various jet Reynolds numbers for an unheated disk ($Ra = 0$). The results suggest that as Re_j exceeds certain low level the primary inertia-driven roll appears. The secondary inertia-driven roll is initiated at somewhat higher Re_j. Some inertia-driven vortex rolls at slightly supercritical Re_j are shown in Fig. 4. The results manifest that the inertia-driven rolls are much smaller and weaker for the larger injection pipe (Fig. 4(c) and (d)). More specifically, for $D_j = 10.0$ and 22.1 mm the primary inertia-driven roll respectively appears at $Re_j = 13.6$ and 15.0. Note that near the critical Re_j the roll is relatively small and appears in the region near the chamber top and surrounding the jet (Fig. 4(a) and (d)). It should be mentioned that even for an unheated disk an outer roll also appears in the region near the chamber side (Fig. 4(a) and (b)). This roll is formed by the deflection of the wall–jet flow along the disk by the chamber side. At a higher Re_j this outer roll is smaller and weaker (Fig. 4(b)) due to the radial thickening of the wall–jet flow along the disk and the deflection of the flow at the chamber side is milder. It has nothing to do with buoyancy since $Ra = 0$.

Our flow visualization further shows that the buoyancy-driven roll starts to emerge as the jet Reynolds number is below certain critical level for a given temperature difference between the heated disk and injected air. This is exemplified in Fig. 5. The results indicate that the buoyancy-driven roll in the outer zone of the

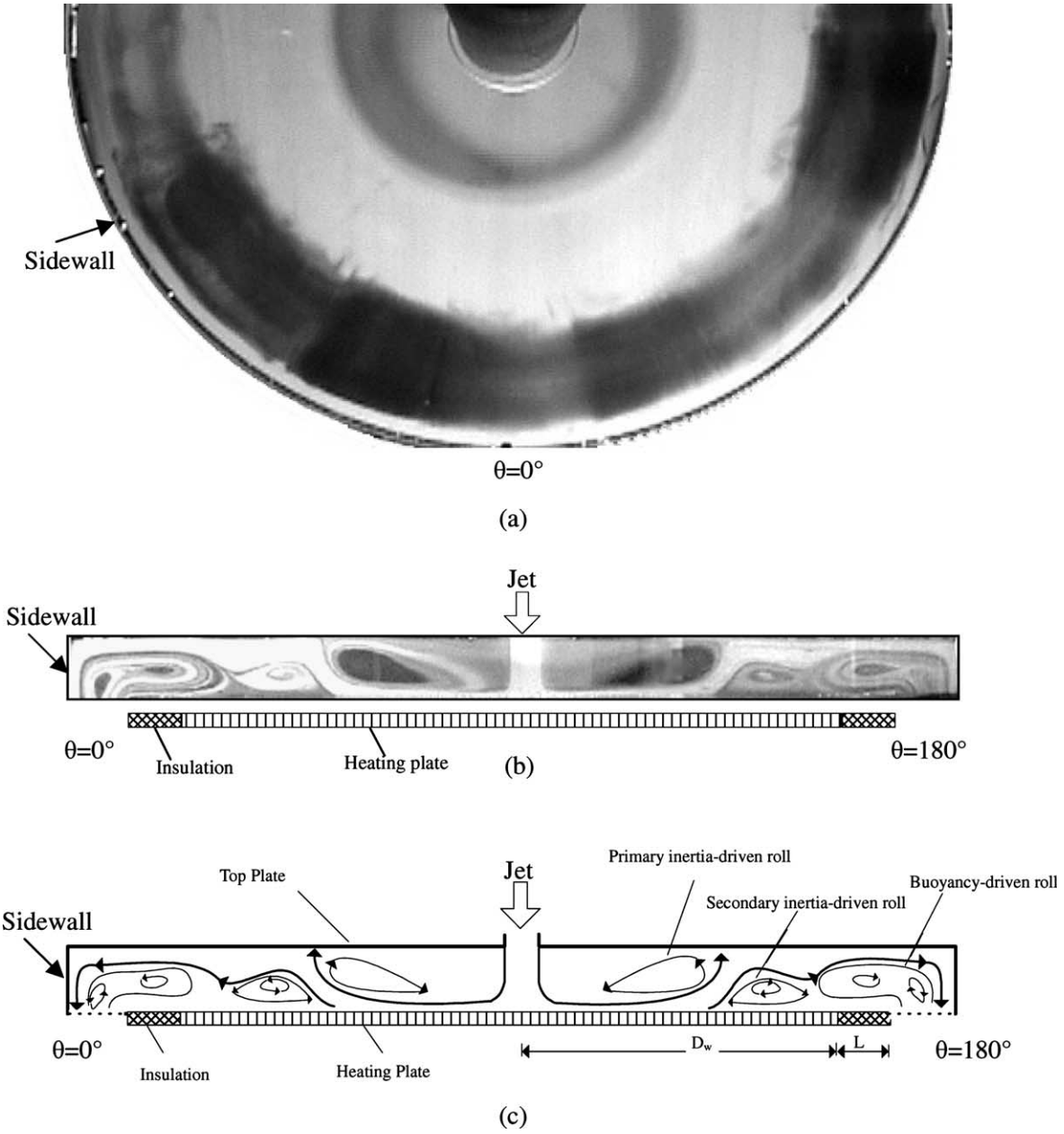

Fig. 3. Steady vortex flow pattern for $D_j = 10$ mm at $Re_j = 406$ ($Q_j = 3.0$ slpm) and $Ra = 7,440$ ($\Delta T = 9.9$ °C): (a) top view flow photo taken at middle horizontal plane halfway between the pipe exit and heated disk, (b) side view flow photo taken at the vertical plane $\theta = 0°$ and 180°, and (c) the corresponding schematically sketched cross-plane vortex flow.

chamber decreases in size and strength at increasing Re_j. Moreover, Table 1 summarizes the critical condition for the onset of the buoyancy-driven roll based on the present data. This critical condition is considered to be reached as long as we can barely see the buoyancy-driven roll in the video films recording the images of the vortex rolls. It is of interest to note that for the small injection pipe the critical buoyancy-to-inertia ratio is nearly constant for various cases at

$$(Gr/Re_j^2)_C \approx 0.0045 \tag{3}$$

But for the large injection pipe the ratio is much higher with

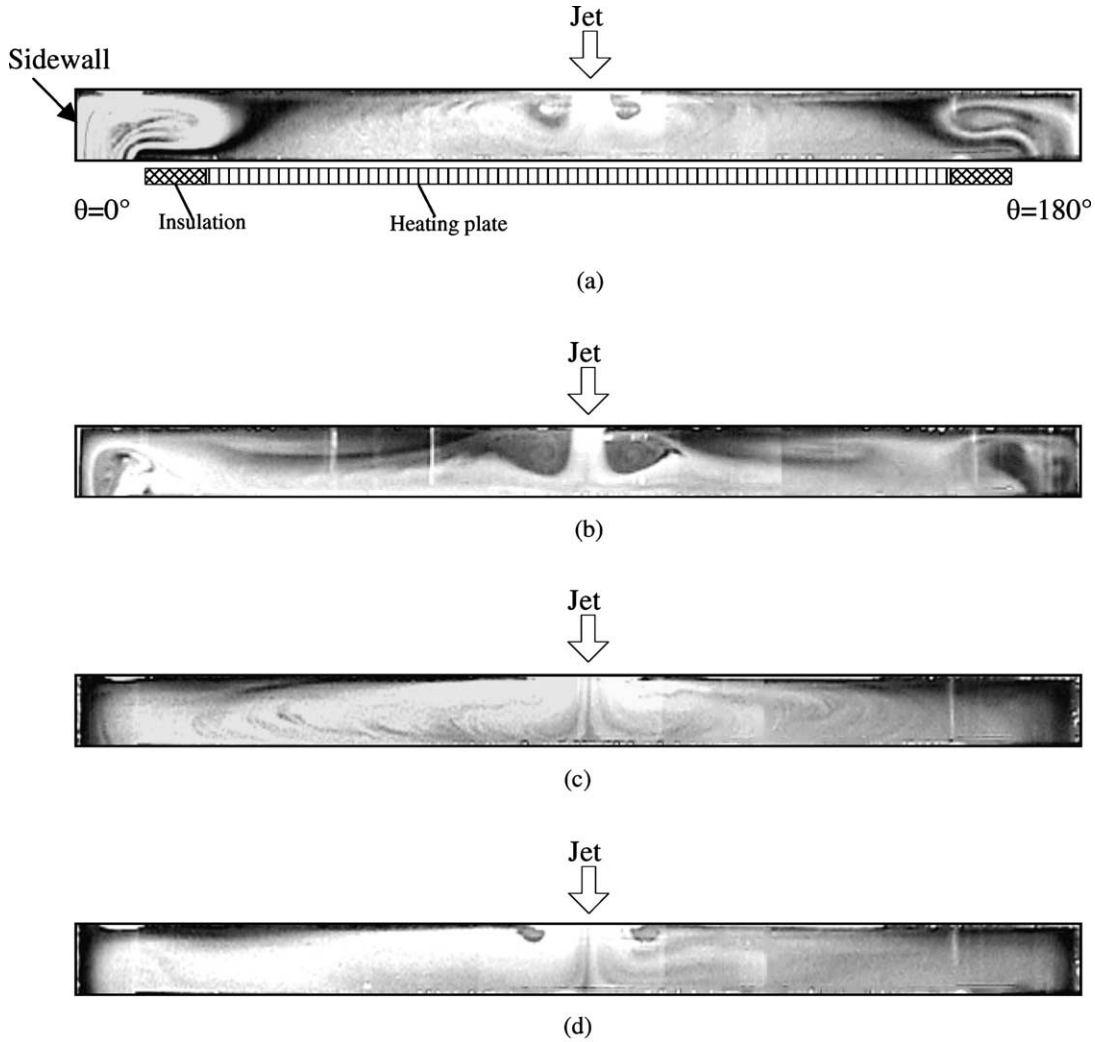

Fig. 4. Steady side view flow photos at low Reynolds numbers for $Ra = 0$: (a) $Re_j = 13.6$ and $D_j = 10.0$ mm ($D_j/H = 0.5$), (b) $Re_j = 20.0$ and $D_j = 10.0$ mm ($D_j/H = 0.5$), (c) $Re_j = 12.0$ and $D_j = 22.1$ mm ($D_j/H = 1.105$), and (d) $Re_j = 15.0$ and $D_j = 22.1$ mm ($D_j/H = 1.105$).

$$(Gr/Re_j^2)_C \approx 0.02 \quad (4)$$

3.3. Effects of jet Reynolds number

How the jet Reynolds number affects the long time gas flow pattern in the processing chamber is manifested in Fig. 6 by presenting the steady side view flow photos for the cross-plane $\theta = 0°$ and 180° for selected Re_j at a low Ra. The results in Fig. 6(a) for the small injection pipe indicate that at this low buoyancy the flow is still dominated by the three vortex rolls as the typical flow pattern (Fig. 3). Besides, at increasing Re_j the two inertia-driven rolls grow in size and intensity with the accompanying decay of the buoyancy-driven roll. Note that in the chamber with the large injection pipe the inertia-driven rolls are smaller and weaker than those with the small injection pipe at the same flow rate. This directly results from the fact that the jet Reynolds number is inversely proportional to the injection pipe diameter at fixed Q_j, according to Eq. (1). Thus for the large injection pipe Re_j is much lower in the present study. It is worth mentioning that the relative strength of vortex rolls is deduced qualitatively from visualizing the motion of smoke particles in the corresponding rolls.

3.4. Effects of Rayliegh number

The effects of the Rayleigh number on the recirculating flow patterns in the chamber are illustrated in

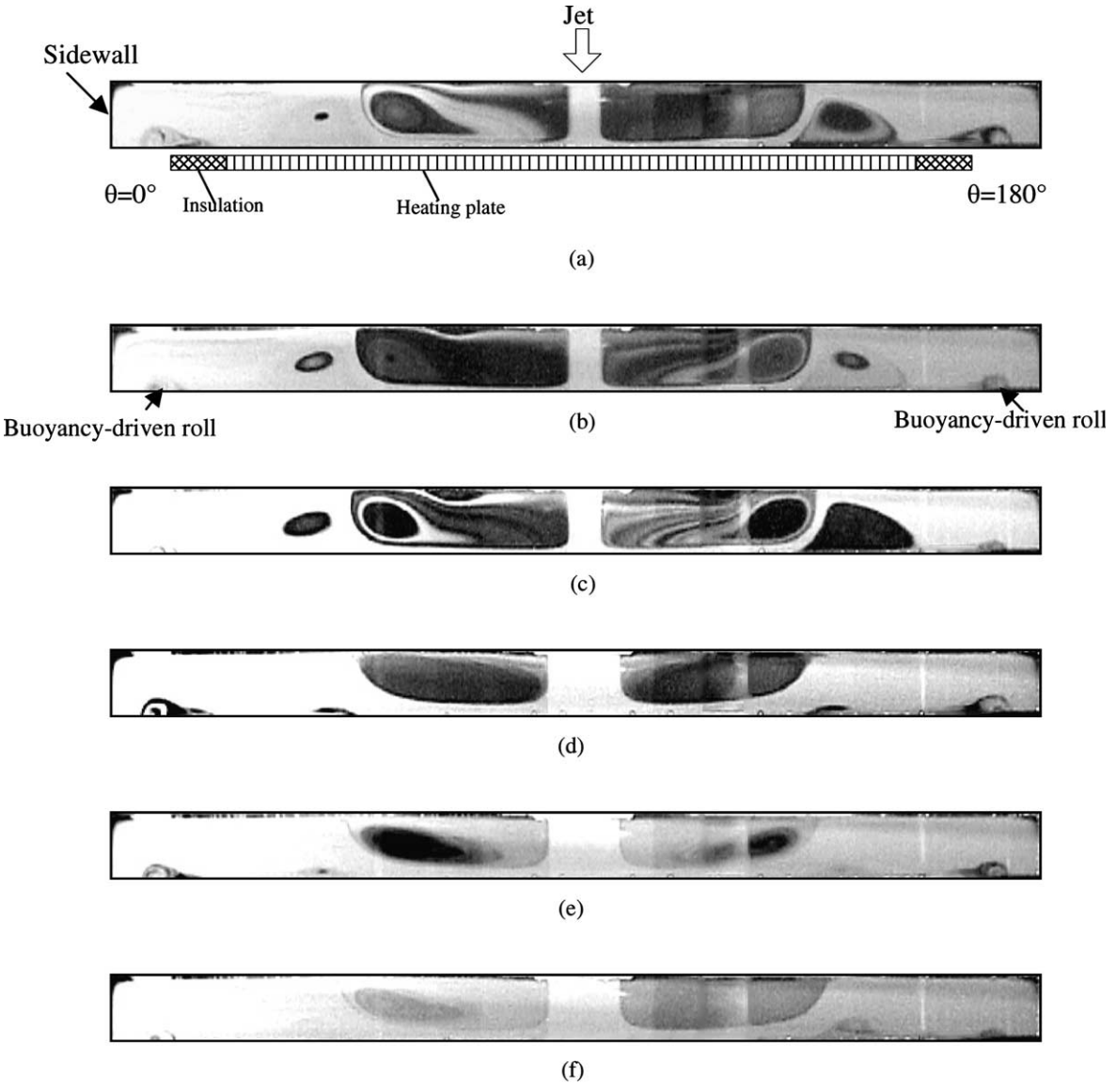

Fig. 5. Steady side view flow photos near the critical condition showing the flow near the onset of buoyancy-driven roll for $Ra = 1,650$ ($\Delta T = 2.2$ °C) with (a) $Re_j = 612$ and $D_j = 10.0$ mm ($D_j/H = 0.5$), (b) $Re_j = 680$ and $D_j = 10.0$ mm ($D_j/H = 0.5$), (c) $Re_j = 748$ and $D_j = 10.0$ mm ($D_j/H = 0.5$), (d) $Re_j = 275$ and $D_j = 22.1$ mm ($D_j/H = 1.105$), (e) $Re_j = 305$ and $D_j = 22.1$ mm ($D_j/H = 1.105$), and (f) $Re_j = 336$ and $D_j = 22.1$ mm ($D_j/H = 1.105$).

Fig. 7 by showing the steady side view flow photos for various Ra at a given Q_j. We first note from the results for the unheated disk ($Ra = 0$) that the outer roll due to the flow deflection at the chamber side is rather small and weak for the large injection pipe (Fig. 7(b)). As the disk becomes heated, the buoyancy-driven roll grows significantly in size and intensity with the Rayleigh number. Note that in the chamber installed with the small injection pipe the buoyancy-driven roll at certain high Ra can be large enough to merge with the secondary inertia-driven roll (Fig. 7(a) at $Ra = 15,030$). But the primary inertia-driven inner roll is only slightly affected by the change in the Rayleigh number. The situation is somewhat different for the large injection pipe due to the absence of the secondary inertia-driven roll (Fig. 7(b)). More specifically, the size growth of the buoyancy-driven roll with Ra is milder for the large injection pipe. Additionally, some size growth of the inertia-driven roll with Ra occurs.

The effects of the injection pipe diameter on the vortex flow pattern can also be seen from comparing the results in Fig. 7(a) with those in Fig. 7(b). The

Table 1
Critical condition for the onset of buoyancy-driven roll for (a) $D_j = 10.0$ mm and (b) $D_j = 22.1$ mm

ΔT (°C)	Flow rate (slpm)	Gr	Re_j	Gr/Re_j^2
(a) $D_j = 10.0$ mm				
2.2	5.5	2360	744	0.0043
3.2	6.5	3440	879	0.0044
4	7	4300	947	0.0048
5	8	5370	1082	0.0046
(b) $D_j = 22.1$ mm				
2.2	5.5	2360	337	0.021
3.2	6.5	3440	398	0.020
4	7.5	4300	459	0.020
5	8.5	5370	520	0.020

comparison manifest that for the large injection pipe the primary inertia-driven roll is weaker to a certain degree and the buoyancy-driven roll is smaller. Besides, for the small injection pipe the merging of the buoyancy-driven roll and secondary inertia-driven roll occurs at some intermediate buoyancy-to-inertia ratio.

To quantify the effects of the governing parameters on the vortex flow characteristics, the data for the maximum radial extent of the inner roll S_I, the maximum height of the outer roll S_O, and the radial location of the center of the secondary roll r_s, are measured from the steady side view flow photos for various cases. The results from this measurement indicate that for the small injection pipe S_I increases almost linearly with the jet Reynolds number for a given Ra, so does the radial location of the middle roll. However, S_O decreases due to an increase in Re_j. We also note that the increase in the size of the inner and outer rolls with the Rayleigh number can be substantial at low Ra especially for the large injection pipe. To facilitate the flow design in the practical application, empirical equations are found to correlate the above data. They can be expressed as

(a) for $D_j = 10.0$ mm

$$\frac{S_I}{D_j} = 3.59 + 0.00521\,Re_j + 4.68\left(\frac{Gr}{Re_j^2}\right) \tag{5}$$

$$\frac{S_O}{H} = 0.792 + 0.00896\,Re_j^{1/2} - 0.0615\left(\frac{Gr}{Re_j^2}\right)^{-1/2} \tag{6}$$

$$\frac{r_s}{D_j} = 5.18 + 0.00426\,Re_j + 9.65\left(\frac{Gr}{Re_j^2}\right) \tag{7}$$

(b) for $D_j = 22.1$ mm

$$\frac{S_I}{D_j} = -1 + 0.236\,Re_j^{1/2} + 1.62\left(\frac{Gr}{Re_j^2}\right)^{1/2} \tag{8}$$

$$\frac{S_O}{H} = 0.848 + 0.00741\,Re_j^{1/2} - 0.121\left(\frac{Gr}{Re_j^2}\right)^{-1/2} \tag{9}$$

When compared with the present data, the standard deviations of Eqs. (5)–(9) are respectively 4%, 4%, 4%, 8.2%, and 5%.

3.5. Temporal characteristics of vortex flows

It is noted from the present experiment that some vortex flows do not reach steady state at long time when the buoyancy-to-inertia ratio is raised to a certain high level and the flows become time dependent. This normally occurs at low jet Reynolds number. The characteristics of a typical time periodic vortex flow are exemplified first in Fig. 8 for both injection pipes by showing the cross-plane flow at certain time instant and the time records of air temperature at selected locations in the processing chamber in the statistical state. We should first recall that at low Re_j only the primary inertia-driven inner and buoyancy-driven outer rolls exist in the chamber. The secondary inertia-driven middle roll does not appear. Now the results in Fig. 8 clearly show that two additional circular rolls are induced in the time periodic vortex flow. These two new rolls are smaller and appear in the middle portion of the chamber right between the inner and outer rolls. Besides, the time periodic vortex flow is slightly asymmetric. The data for the time records given in Fig. 8 indicate that only in the region dominated by the new rolls the air temperature oscillates significantly with time. Elsewhere the temperature oscillation is small. A close inspection of the time records reveals that the mean air temperature is much higher in the region dominated by the new rolls than that in the buoyancy-driven region. This can be attributed to the fact that upon impinging the disk the air jet is forced to mainly move in the near wall region along the disk due to the presence of the primary inertia-driven roll. The wall-jet flow gradually gets heated as it moves radially outwards before retarded by the buoyancy-driven roll. Thus the air temperature is highest in the region between the inner and outer rolls.

To further reveal the temporal characteristics of the time periodic vortex flow, the time records of the air temperature and the corresponding power spectrum densities (PSD) are presented next in Fig. 9 for various Re_j at $Ra = 15{,}030$ for $D_j = 22.1$ mm. The PSD are evaluated from the Fourier analysis of the measured data. The results clearly manifest that the flow oscillates at larger amplitude and slightly lower frequency for a lower Re_j at a fixed Ra. This trend is apparently owing to

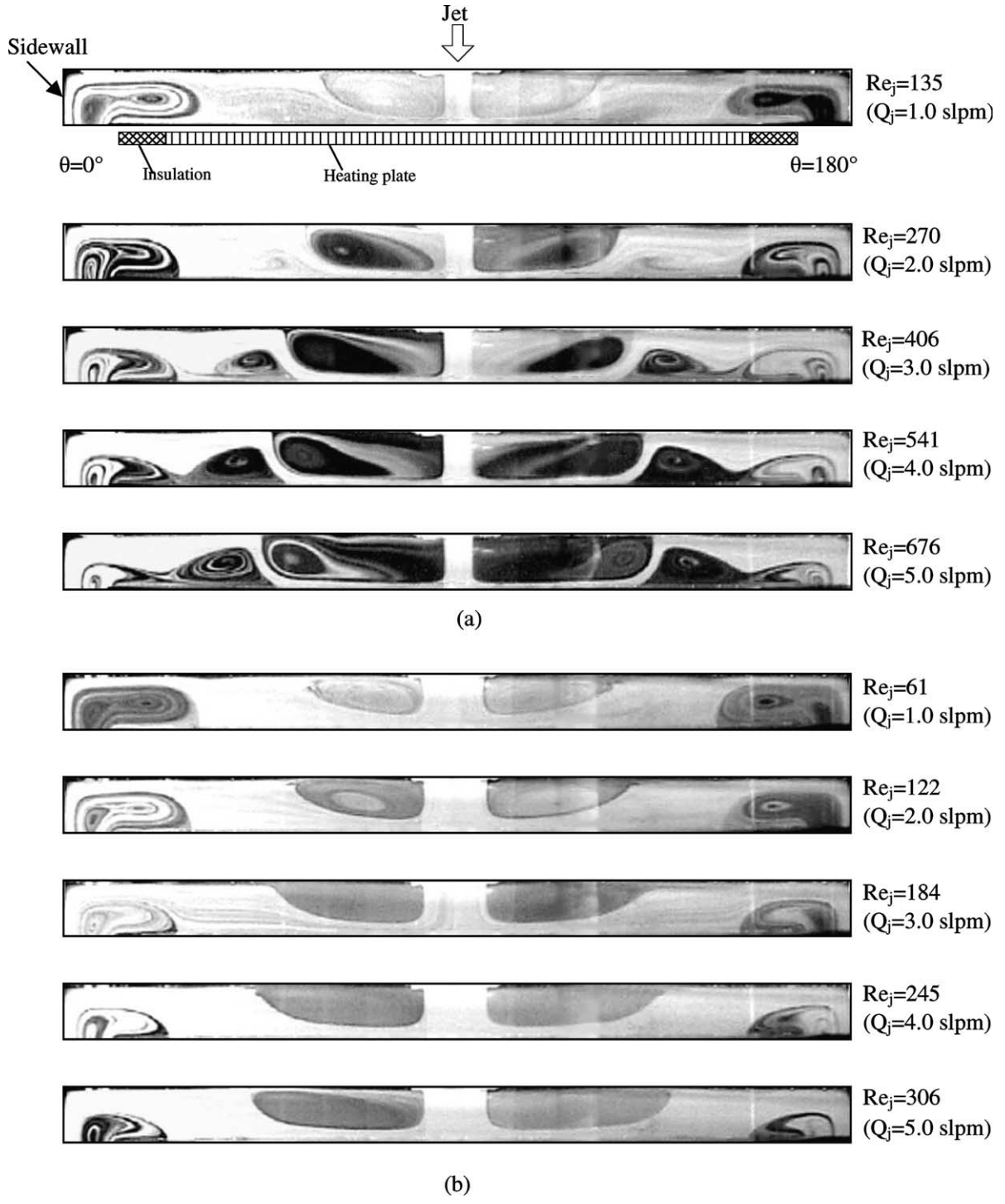

Fig. 6. Steady side view flow photos taken at the cross-plane $\theta = 0$ and 180° for various jet Reynolds numbers at $Ra = 3830$ ($\Delta T = 5.1$ °C) for D_j = (a) 10.0 mm ($D_j/H = 0.5$) and (b) 22.1 mm ($D_j/H = 1.105$).

the accompanying rise in the buoyancy-to-inertia ratio. Note that the time periodic flow prevails over a finite noticeable range of the Reynolds number (Fig. 9(b)–(d)) and the flow oscillation is characterized by a single

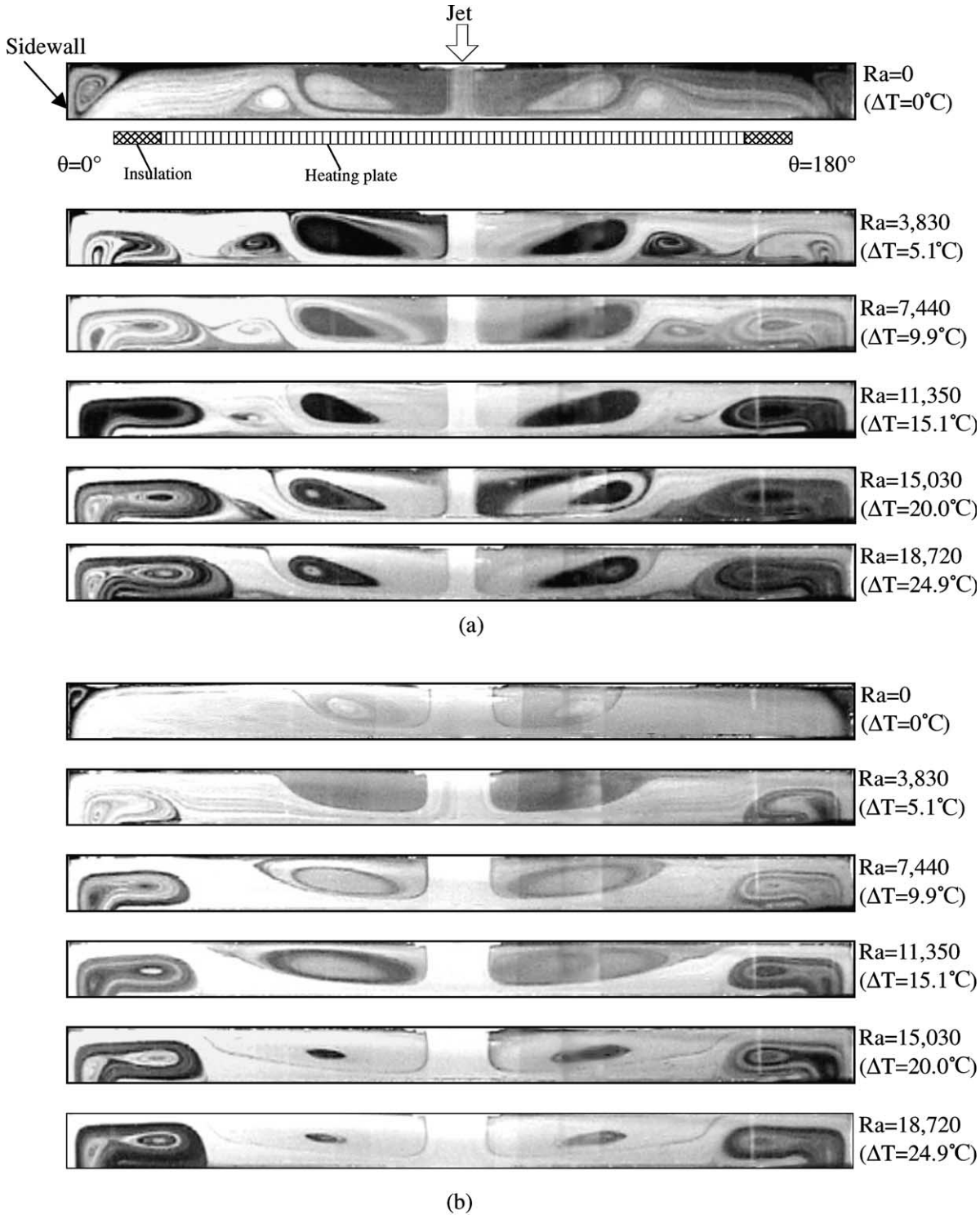

Fig. 7. Steady side view flow photos taken at the cross-plane $\theta = 0°$ and 180° for various Rayleigh numbers at $Q_j = 3.0$ slpm for $D_j =$ (a) 10.0 mm ($D_j/H = 0.5$) and $Re_j = 406$ and (b) 22.1 mm ($D_j/H = 1.105$) and $Re_j = 184$.

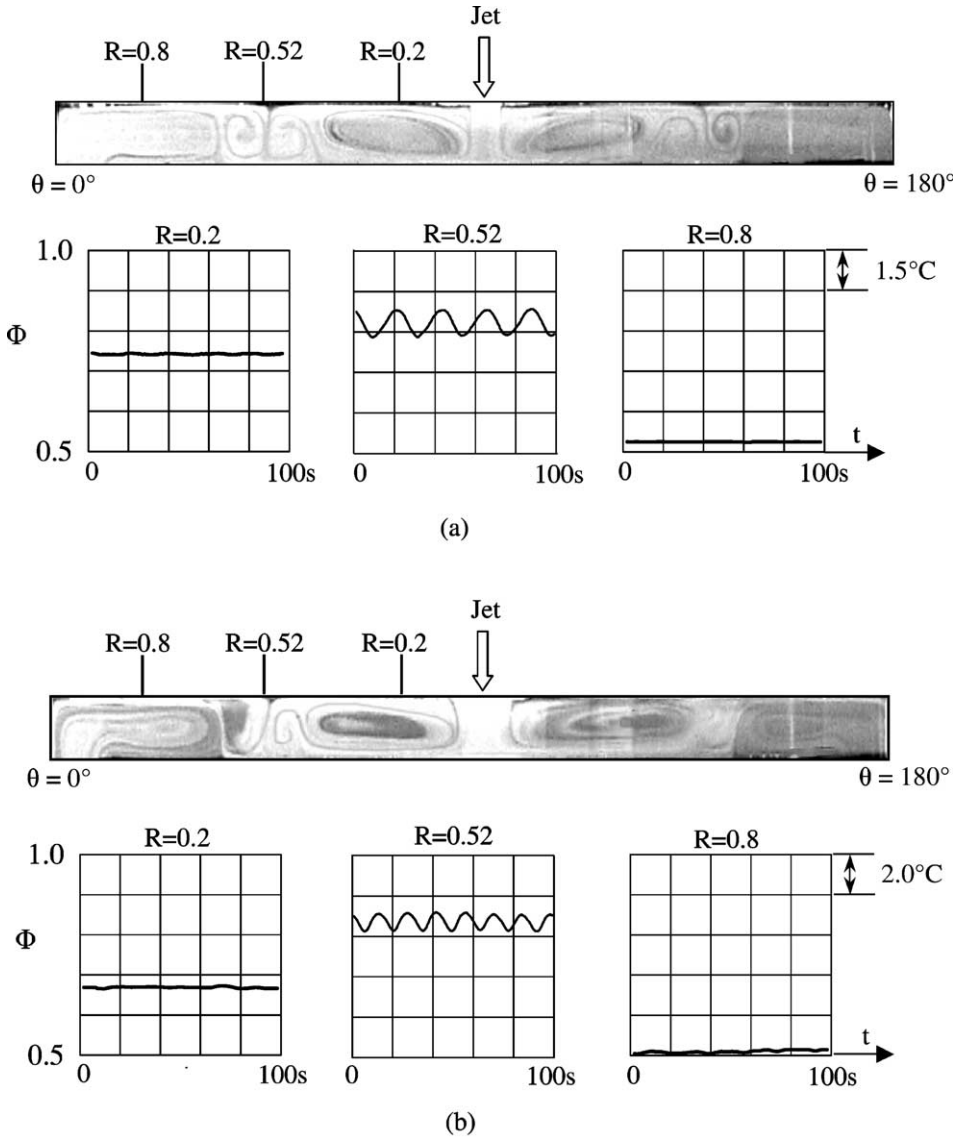

Fig. 8. Side view flow photos at the cross-plane $\theta = 0°$ and 180° at certain time instant in a typical periodic cycle and time records of air temperature at selected locations in the middle horizontal plane $Z = 0.5$ for (a) $Re_j = 136$, $Ra = 11{,}350$ and $D_j = 10.0$ mm ($t_p = 21.1$ s) ($Gr/Re_j^2 = 0.61$ and $D_j/H = 1.105$) and (b) $Re_j = 61$, $Ra = 15{,}030$ and $D_j = 22.1$ mm ($t_p = 13.8$ s) ($Gr/Re_j^2 = 4.03$ and $D_j/H = 1.105$).

fundamental frequency. At certain low Re_j (high Gr/Re_j^2) the flow oscillation becomes quasi-periodic in time and second fundamental frequency sets in (Fig. 9(a)).

The effects of the Rayleigh number on the temporal characteristics of the time periodic vortex flow are also examined. The results indicate that the oscillation amplitude of the air temperature is only slightly affected by the variation in the Rayleigh number. The corresponding PSDs suggest that the flow oscillates at a slightly lower (higher) frequency for a higher Rayleigh number for the larger (smaller) injection pipe. Based on the present data, the oscillation frequency of the buoyancy-driven time periodic vortex flow in the processing chamber with the large injection pipe can be correlated as

$$F = \frac{f}{(\alpha/H^2)} = -0.231 + 0.0183\,Re_j + 5453\,Ra^{-1} \qquad (10)$$

while for the small injection pipe

$$F = \frac{f}{(\alpha/H^2)} = 0.0203 + 0.0105\,Re_j - 6045\,Ra^{-1} \qquad (11)$$

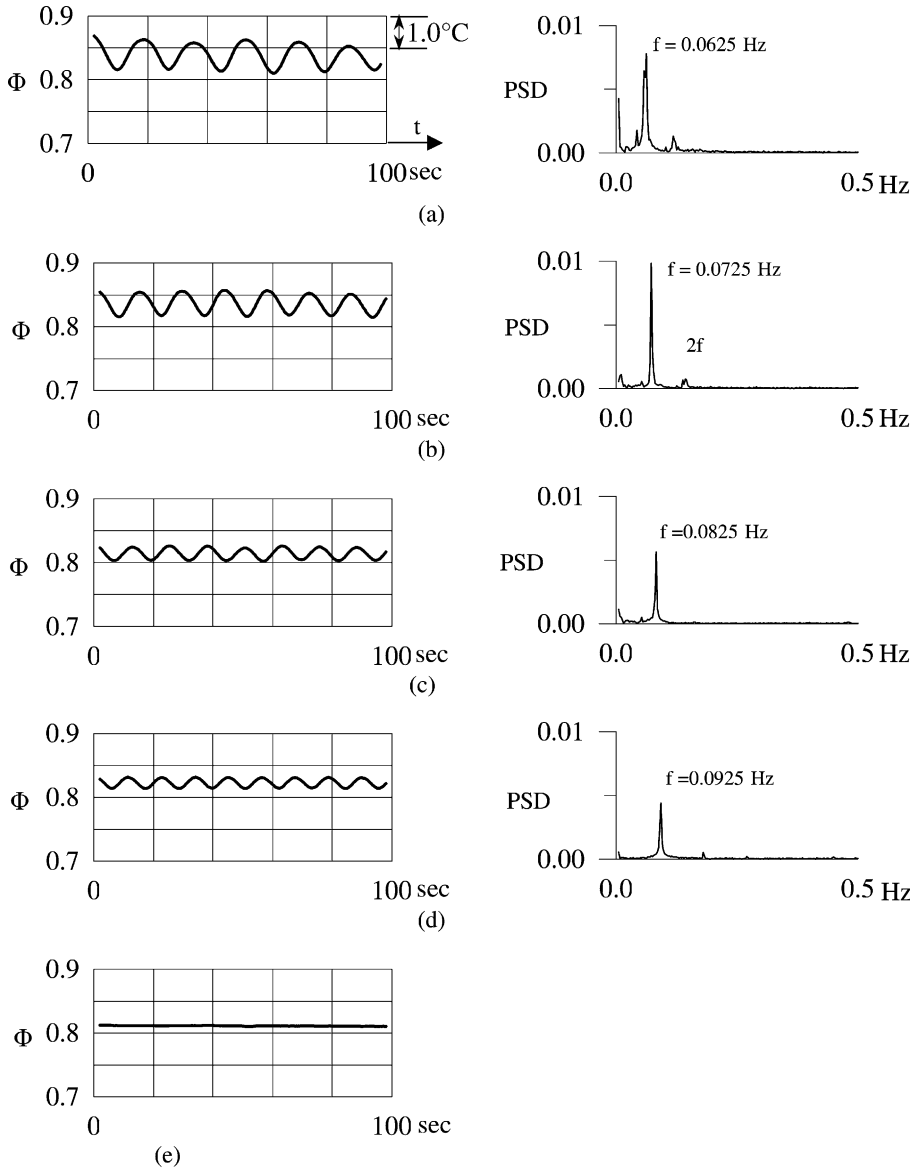

Fig. 9. The time records of nondimensional air temperature and the corresponding PDS for $Ra = 15{,}030$ and $D_j = 22.1$ mm at location $(R, Z) = (0.52, 0.5)$ for $\theta = 0°$ for various jet Reynolds numbers Re_j = (a) 49, (b) 61, (c) 73, (d) 85 and (e) 98.

Both equations can predict our data with a standard deviation less than 5%.

It is of interest to explore the temporal evolution of the time periodic vortex flow. This is illustrated in Fig. 10 by showing the side view flow photos and the corresponding schematically sketched vortex flow patterns at the cross-plane $\theta = 0°$ at selected time instants in a typical periodic cycle for the case with $Re_j = 61$ and $Ra = 11{,}350$ for $D_j = 22.1$ mm. Note that in the beginning of the cycle designated as time $t = 0$ s we only have two big vortex rolls in the processing chamber, one primary inertia-driven roll in the core region of the chamber and another buoyancy-driven roll near the chamber side. Shortly later at $t = 1$ s a weak and small thermal plume rises from the heated copper plate in the region below the outer portion of the inertia-driven roll, causing this portion of the roll to become elongated in the radial direction. The thermal plume then grows quickly with time and a slender neck is formed between the outer and main portions of the inertia-driven roll. As this process continues, it is observed that at $t = 3$ s the outer portion splits from the main portion of the roll

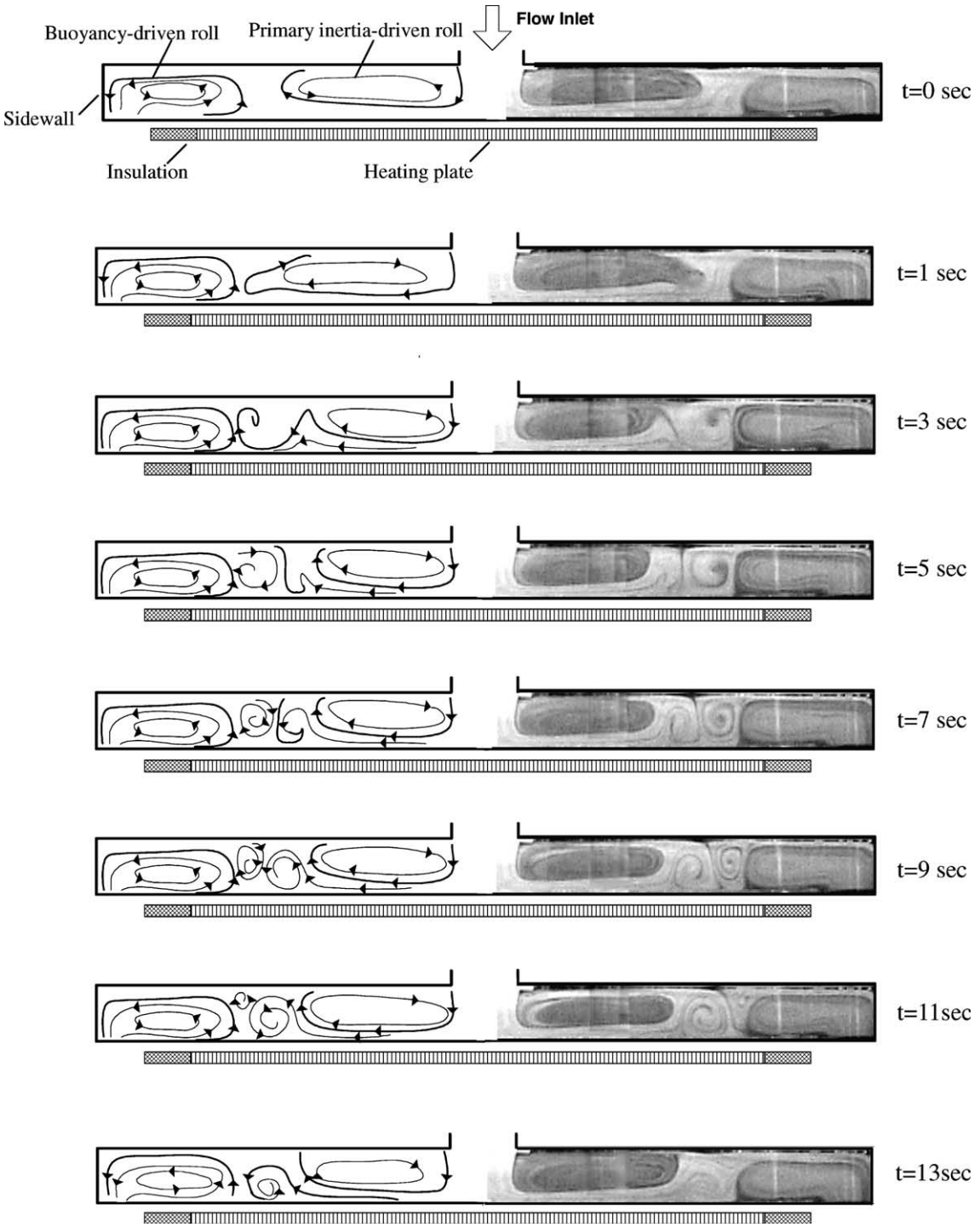

Fig. 10. Side view flow photos taken at the cross-plane $\theta = 0°$ for $Re_j = 61$, $Ra = 11{,}350$ and $D_j = 22.1$ mm at selected time instants (right) and the corresponding schematically sketched cross-plane flow (left) in a typical periodic cycle ($t_p = 13.3$ s).

and a new circular vortex roll is generated in the region between the two big rolls. For a further increase in time the new roll strengthens gradually. Meanwhile the thermal plume grows slowly and evolves into another

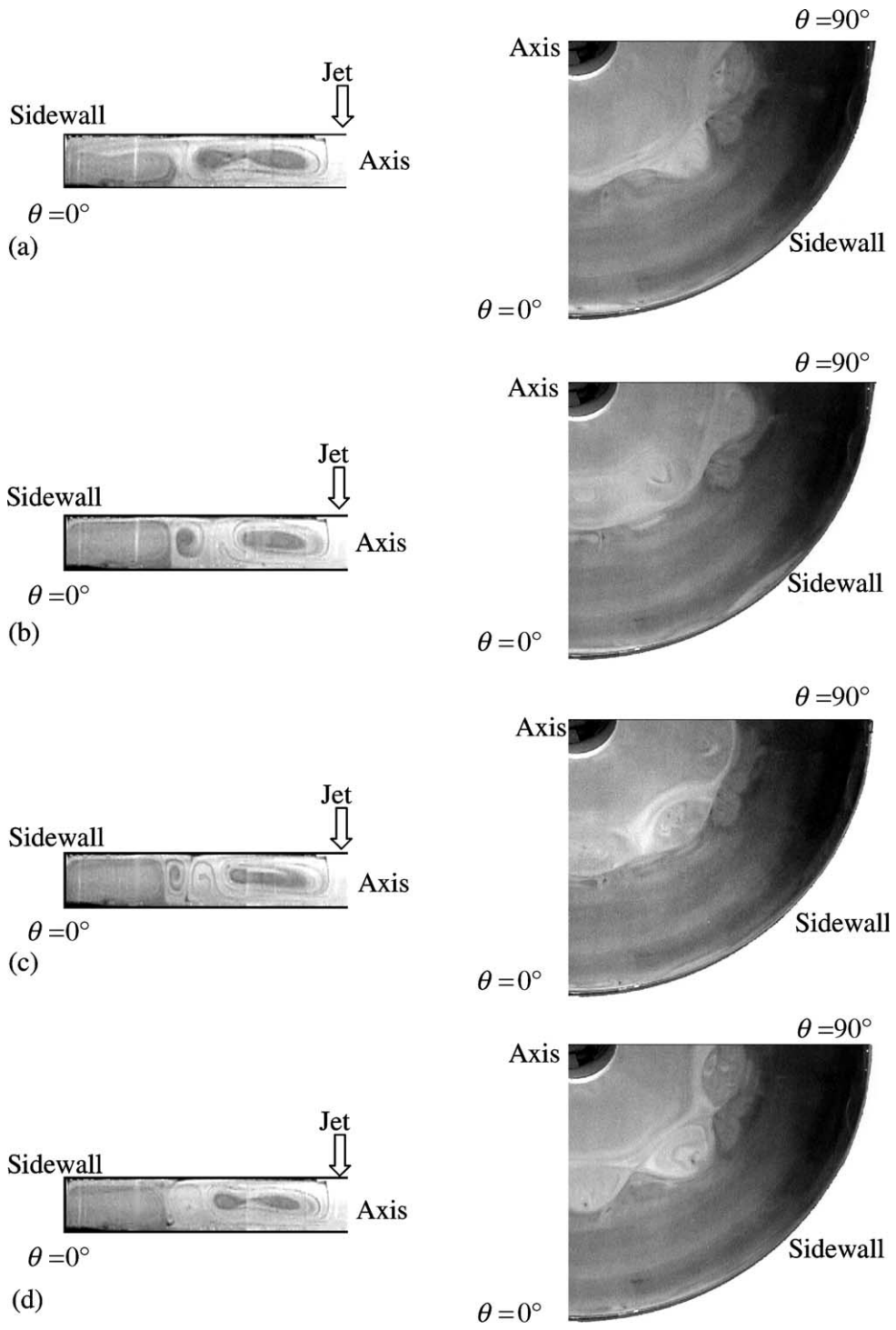

Fig. 11. Side view flow photos taken at $\theta = 0°$ (left) and a quarter of top view flow photos (right) taken at middle horizontal plane with $Re_j = 61$, $Ra = 11{,}350$ and $D_j = 22.1$ mm at selected time instants in statistical state for (a) $t = 0$ s, (b) $t = 5$ s, (c) $t = 9$ s and (d) $t = 13$ s.

new circular vortex roll, as evident from the flow photos at $t = 7$ and 9 s. Thus, two additional rolls appear and there are four circular rolls in the processing chamber in this period of time. It is important to note that as the process keeps going, the roll resulting from the splitting of the inertia-driven roll begins to decay. Later the new roll evolving from the thermal plume decays quickly and at $t = 11$ s it becomes very small. At $t = 13$ s it is already very weak and nearly disappears. Finally at the end of the cycle at $t = t_p = 13.3s$, the two new rolls disappear completely and we only have two big rolls in the chamber.

To reveal the complete picture of the complex time periodic vortex flow structure, the top view flow photos taken at $Z = 0.5$ along with the side view flow photos taken at the cross-plane $\theta = 0°$ for the typical case are presented in Fig. 11 at selected time instants in a typical periodic cycle. The results clearly show that the vortex flow does not possess axisymmetry and exhibits a significant circumferential variation. In fact, the cross-sections of the two new rolls vary circumferentially to such a large degree that each roll is in the form of large connecting blobs. The blobs are essentially the flow recirculations and connect through narrow necks. Besides, the blobs in the same roll do not have the same size and circulation strength.

3.6. Flow regime map

Based on the present data, a flow regime map delineating the temporal state of the inertia- and buoyancy-driven flow in the processing chamber is shown in Fig. 12 in terms of $Ra(D_j/H)^{-0.3}$ vs. $Re_j(D_j/H)$. The results in this plot manifest that when the jet Reynolds number Re_j and/or the aspect ratio of the processing chamber D_j/H are high so that $Re_j(D_j/H) \geqslant 200$, the buoyancy-to-inertia ratio in the flow is low for the range of the Rayleigh number considered here and we have stable vortex flow. But when $Re_j(D_j/H)$ is below 200, the vortex flow becomes time periodic as $Ra(D_j/H)^{-0.3}$ exceeds certain level. For a further raise in Ra the flow can evolve to a quasi-periodic state. Finally, for a high buoyancy-to-inertia ratio the vortex flow shows a random variation with time. More specifically, the boundary between the quasi-periodic and chaotically unstable vortex flow can be correlated as

$$Ra \times \left(\frac{D_j}{H}\right)^{-0.3} = 10716 + 10\left[Re_j \times \left(\frac{D_j}{H}\right)\right]^{1.5} \tag{12}$$

In addition, the transition from the steady to time-periodic vortex flow occurs when

$$Ra \times \left(\frac{D_j}{H}\right)^{-0.3} = 2386 + 0.57\left[Re_j \times \left(\frac{D_j}{H}\right)\right]^{2} \tag{13}$$

These two correlations are also shown in Fig. 12.

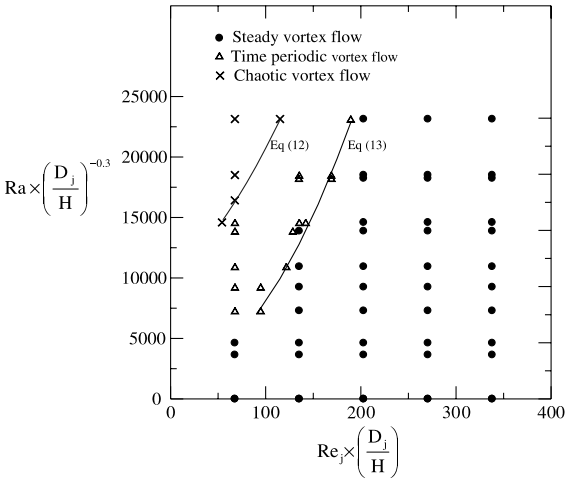

Fig. 12. Flow region map delineating the temporal state of the vortex flow.

4. Concluding remarks

Combined experimental flow visualization and transient temperature measurement have been conducted in the present study to explore the onset, steady and time dependent vortex flow characteristics associated with a low speed gas jet impinging onto a circular heated disk confined in a vertical adiabatic cylindrical chamber. Effects of the jet flow rate, temperature difference between the heated disk and cold air jet, and diameter of the injection pipe on the vortex flow structures were inspected in detail. The major results obtained here can be briefly summarized in the following:

1. The typical steady vortex flow consists of an inertia-driven circular roll around the jet axis and a buoyancy-driven roll near the chamber side. At high jet Reynolds numbers a secondary inertia-driven roll appears. The size of the inertia-driven rolls increases significantly with Re_j. The conditions leading to the onset of the inertia and buoyancy-driven rolls are found.
2. At a certain high Richardson number with $Gr/Re_j^2 \geqslant 0.19$ for $D_j = 10.0$ mm and $Gr/Re_j^2 \geqslant 1.15$ for $D_j = 22.1$ mm the vortex flow becomes time periodic and two new vortex rolls are induced due to an additional thermal plume rising from the heated disk and splitting of the inertia driven roll. In the region occupied by the two new rolls, the vortex flow oscillates significantly with time. Besides, the oscillation frequency of the flow increases noticeably with Re_j.

3. Empirical equations are proposed to correlate the size and position of the steady vortex rolls and the oscillation frequency of the time-periodic vortex flow.
4. A flow regime map is given to delineate the temporal state of the vortex flow.

During the course of this investigation it is realized that the processes through which the vortex rolls are formed during the initial transient stage are of academic and practical interest. The problem will be examined in the future.

Acknowledgements

The financial support of this study by the Engineering Division of Energy Committee and National Science Council of Taiwan, ROC is greatly appreciated.

References

[1] S. Polat, B. Huang, A.S. Mujumdar, W.J.M. Douglas, Numerical flow and heat transfer under impinging jets: a review, in: C.L. Tien, T.C. Chawla (Eds.), Annular Review of Numerical Fluid Mechanics and Heat Transfer 2, Hemisphere, Washington, DC, 1989, pp. 157–197.
[2] G.B. Stringfellow, Organometallic Vapor Phase Epitaxy: Theory and Practice, Academic Press, San Diego, 1989 (Chapter 5).
[3] S.A. Campbell, The Science and Engineering of Microelectronic Fabrication, Oxford University Press, New York, 1996 (Chapter 6).
[4] M.L. Hitchamn, K.F. Jensen, Chemical Vapor Deposition (Principle and Application), Academic Press, San Diego, 1993 (Chapter 2).
[5] T.C. Cheng, P.H. Chiou, T.F. Lin, Visualization of mixed convective vortex rolls in an impinging jet flow of air through a cylindrical chamber, Int. J. Heat Mass Transfer 45 (2002) 3357–3368.
[6] M.T. Scholtz, O. Trass, Mass transfer in a nonuniform impinging jet, AIChE J. 16 (1970) 90–96.
[7] E.M. Sparrow, T.C. Wong, Impingment transfer coefficients due to initially laminar slot jets, Int. J. Heat Mass Transfer 18 (1975) 597–605.
[8] J.H. Masliyah, T.T. Nguyen, Mass transfer due to an impinging slot jet, Int. J. Heat Mass Transfer 22 (1979) 237–244.
[9] P. Hrycak, Heat transfer from round impinging jets to a flat plate, Int. J. Heat Mass Transfer 26 (1983) 1857–1865.
[10] İ.B. Özdermir, J.H. Whitelaw, Impingement of an axisymmetric jet on unheated and heated flat plates, J. Fluid Mech. 240 (1992) 503–532.
[11] T. Liu, J.P. Sullivan, Heat transfer and flow structures in an excited circular impinging jet, Int. J. Heat Mass Transfer 39 (1996) 3695–3706.
[12] N.R. Saad, W.J.M. Douglas, A.S. Mujumdar, Prediction of heat transfer under an axisymmetric laminar impinging jet, Int. Eng. Chem. Fundam. 16 (1977) 148–154.
[13] H.S. Law, J.H. Masliyah, Mass transfer due to a confined laminar impinging axisymmetric jet, Int. Eng. Chem. Fundam. 23 (1984) 446–454.
[14] M. Behnia, S. Parneix, Y. Shabany, P.A. Durbin, Numerical study of turbulent heat transfer in confined and unconfined impinging jets, Int. J. Heat Fluid Flow 20 (1999) 1–9.
[15] L.P. Chua, S.C.M. Yu, H.-S. Li, Flow visualization and preliminary measurements of a confined jet with and without target, Int. Commun. Heat Mass Transfer 27 (2000) 191–200.
[16] P.R. Voke, S. Gao, Numerical study of heat transfer from an impinging jet, Int. J. Heat Mass Transfer 41 (1998) 671–680.
[17] J.A. Fitzgerald, S.V. Garimella, A study of the flow field of a confined and submerged impinging jet, Int. J. Heat Mass Transfer 41 (1998) 1025–1034.
[18] V.A. Marple, B.Y.H. Liu, K.T. Whitby, On the flow fields of inertial impactors, Trans. ASME, J. Fluids Eng. (1974) 394–400.
[19] S. Ashforth-Forst, K. Jambunathan, C.F. Whitney, Velocity and turbulence characteristics of a semi-confined orthogonally impinging slot jet, Exp. Thermal Fluid Sci. 14 (1997) 60–67.
[20] H.S. Law, J.H. Masliyah, Numerical prediction of the flow field due to a confined laminar two-dimensional submerged jet, Comput. Fluids 12 (1984) 199–215.
[21] V.A. Chiriac, A. Ortega, A numerical study of the unsteady flow and heat transfer in a transitional confined slot jet impinging on an isothermal surface, Int. J. Heat Mass Transfer 45 (2002) 1237–1248.
[22] R. Viskanta, Heat transfer to impinging isothermal gas and flame jets, Exp. Thermal Fluid Sci. 6 (1993) 111–134.
[23] K. Jambunathan, E. Lai, M.A. Moss, B.L. Button, A review of heat transfer data for single circular jet impingement, Int. J. Heat Fluid Flow 13 (1992) 106–115.
[24] G. Wahl, Hydrodynamic description of CVD processes, Thin Solid Films 40 (1977) 13–26.
[25] A.H. Dilawari, J. Szekely, A mathematical representation of a modified stagnation flow reactor for MOCVD application, J. Cryst. Growth 108 (1991) 491–498.
[26] P.N. Gadgil, Optimization of a stagnation point flow reactor design for metalorganic chemical vapor deposition by flow visualization, J. Cryst. Growth 134 (1993) 302–312.
[27] H.V. Santen, C.R. Kleijn, H.E.A. Van Den Akker, Symmetry breaking in a stagnation-flow CVD reactor, J. Cryst. Growth 212 (2000) 311–323.
[28] S. Chatterjee, I. Trachtenberg, T.F. Edgar, Mathematical modeling of a single-wafer RTP thermal reactor, J. Electrochem. Soc 139 (1992) 3682–3689.
[29] S.J. Kline, F.A. McClintock, Describing uncertainties in single-sample experiment, Mech. Eng. 75 (1953) 3–8.